Inertia-gravity waves in Antarctica: A case study using simultaneous lidar and radar measurements at McMurdo/Scott Base (77.8°S, 166.7°E)

Cao Chen,[1] Xinzhao Chu,[1] Adrian J. McDonald,[2] Sharon L. Vadas,[3] Zhibin Yu,[1] Weichun Fong,[1] and Xian Lu[1]

Received 17 October 2012; revised 25 January 2013; accepted 6 March 2013; published 9 April 2013.

[1] This study presents the first coincident observation of inertia-gravity waves (IGWs) by lidar and radar in the Antarctic mesopause region. This is also the first known observation of two simultaneous IGWs at the same location. An Fe Boltzmann lidar at Arrival Heights (77.8°S, 166.7°E) provides high-resolution temperature data, and a co-located MF radar provides wind data. On 29 June 2011, coherent wave structures are observed in both the Fe lidar temperature and MF radar winds. Two dominant waves are determined from the temperature data with apparent periods of 7.7 ± 0.2 and 5.0 ± 0.1 h and vertical wavelengths of 22 ± 2 and 23 ± 2 km, respectively. The simultaneous measurements of temperature and wind allow the intrinsic wave properties to be derived from hodograph analyses unambiguously. The analysis shows that the longer-period wave propagates northward with an azimuth of $\theta = 11° \pm 5°$ clockwise from north. This wave has a horizontal wavelength of $\lambda_h = 2.2 \pm 0.2 \times 10^3$ km and an intrinsic period of $\tau_I = 7.9 \pm 0.3$ h. The intrinsic horizontal phase speed (C_{Ih}) for this wave is 80 ± 4 m/s, while the horizontal and vertical group velocities (C_{gh} and C_{gz}) are 48 ± 3 m/s and 0.5 ± 0.1 m/s, respectively. The shorter-period wave has $\tau_I = 4.5 \pm 0.3$ h and $\theta = 100° \pm 4°$ with $\lambda_h = 1.1 \pm 0.1 \times 10^3$ km and $C_{Ih} = 68 \pm 5$ m/s. Its group velocities are $C_{gh} = 58 \pm 5$ m/s and $C_{gz} = 1.1 \pm 0.1$ m/s. Therefore, both waves propagate with very shallow elevation angles from the horizon ($\phi = 0.6° \pm 0.1°$ and $\phi = 1.1° \pm 0.1°$ for the longer- and shorter-period waves, respectively) but originate from different sources. Our analysis suggests that the longer-period IGW most likely originates from the stratosphere in a region of unbalanced flow.

Citation: Chen, C., X. Chu, A. J. McDonald, S. L. Vadas, Z. Yu, W. Fong and X. Lu (2013), Inertia-gravity waves in Antarctica: A case study using simultaneous lidar and radar measurements at McMurdo/Scott Base (77.8°S, 166.7°E), *J. Geophys. Res. Atmos.*, *118*, 2794–2808, doi:10.1002/jgrd.50318.

1. Introduction

[2] Gravity waves are critically important in the middle and upper atmosphere because of their role in influencing the mean circulation, affecting thermal structure, and transporting energy, momentum, and constituent [*Fritts and Alexander*, 2003]. Unfortunately, the gravity wave parameterizations used in global models are poorly constrained, and information on the range of intrinsic wave properties observed in the mesosphere and lower thermosphere (MLT) and on the sources of these waves is limited. Long-duration, large-altitude-range and high-resolution measurements of temperature and wind can be used to characterize the intrinsic properties of gravity waves, examine their propagation, and infer the probable sources, thus providing important constraints for gravity wave parameterizations in global circulation models [*Alexander and Rosenlof*, 2003]. Here we examine such temperature and wind perturbations that we believe are caused by inertia-gravity waves (IGWs). These waves have frequencies close to the inertial frequency and are affected by the rotation of the Earth. This class of gravity wave is often observed in the troposphere and lower stratosphere [e.g., *Cot and Barat*, 1986; *Sato*, 1994; *Sato et al.*, 1997; *Thomas et al.*, 1999; *Vincent and Alexander*, 2000; *Guest et al.*, 2000; *Hoffmann et al.*, 2006; *Nastrom and Eaton*, 2006; *Vaughan and Worthington*, 2007], but less frequently in the mesosphere and lower thermosphere [e.g., *Nakamura et al.*, 1993; *Hall et al.*, 1995; *Li et al.*, 2007; *Lu et al.*, 2009; *Nicolls et al.*, 2010]. The infrequent occurrence of these waves in the MLT region was believed to occur because of

[1]Cooperative Institute for Research in Environmental Sciences and Department of Aerospace Engineering Sciences, University of Colorado at Boulder, Boulder, Colorado, USA.
[2]Department of Physics and Astronomy, University of Canterbury, New Zealand.
[3]Northwest Research Associates, Boulder, Colorado, USA.

Corresponding authors: X. Chu and C. Chen, Cooperative Institute for Research in Environmental Sciences (CIRES) and Department of Aerospace Engineering Sciences, University of Colorado at Boulder, 216 UCB, UCB CIRES Boulder, CO 80309-0216, USA. (Xinzhao.Chu@Colorado.edu and Cao.Chen@Colorado.edu)

©2013. American Geophysical Union. All Rights Reserved.
2169-897X/13/10.1002/jgrd.50318

their small vertical wavelengths and small horizontal phase speeds, which make these waves susceptible to critical-level filtering by background winds as they propagate upward [*Nicolls et al*., 2010].

[3] Although they are thought to contribute less to momentum flux transport than smaller-scale waves [*Fritts and Vincent*, 1987], IGWs can play an important role in the Earth's atmosphere; for example, in constituent mixing via turbulence caused by convective and dynamical instability in the wave field [*Fritts and Rastogi*, 1985; *O'Sullivan and Dunkerton*, 1995; *Xu et al*., 2000]. Recently, studies have shown that underestimated gravity wave drag (GWD), ascribed to both IGWs and higher-frequency gravity waves in the polar regions, may be responsible for the long-standing "cold pole" problem in many general circulation and chemistry climate models [e.g., *McLandress et al*., 2012; *Tan et al*., 2011]. IGWs have been observed to induce the formation of polar stratospheric clouds (PSCs), which can cause enhanced ozone depletion in the polar regions [*Dörnbrack et al*., 2002; *Shibata et al*., 2003; *McDonald et al*., 2009]. In the polar mesosphere, recent observations by *Chu et al*. [2011a] have shown that the cold phase of large temperature oscillations induced by IGWs facilitates the formation of polar mesospheric clouds (PMCs). In spite of playing such an important role in the polar regions, information concerning the sources and properties of these gravity waves is still limited as compared to midlatitudes and low latitudes [e.g., *Cot and Barat*, 1986; *Sato*, 1994; *Sato et al*., 1997; *Thomas et al*., 1999; *Vincent and Alexander*, 2000; *Guest et al*., 2000; *Nastrom and Eaton*, 2006; *Vaughan and Worthington*, 2007; *Nakamura et al*., 1993; *Hall et al*., 1995; *Li et al*., 2007; *Lu et al*., 2009]. Therefore, investigations of IGWs in the mesopause region over the Antarctic are important, due to their potential influence on MLT temperatures and dynamics.

[4] In the Antarctic MLT, there are a few observations of near-inertial frequency oscillations [e.g., *Hernandez et al*., 1992, 1993; *Collins et al*., 1992; *Fritts et al*., 1998]. Among these authors, *Hernandez et al*. [1993] have hinted these oscillations might be IGWs, while others indicate a tidal or planetary wave origination. Characterization and climatology of the gravity wave motions observed in the Antarctic MLT were reported by *Collins et al*. [1994] and *Collins and Gardner* [1995] using a sodium lidar, and by *Vincent* [1994] using an MF radar. However, the current report is the first study that derives the intrinsic properties of IGWs in the Antarctic MLT. A new lidar campaign at McMurdo, Antarctica, has begun to show an unexpectedly high occurrence of waves with periods of 4–9 h in the MLT temperatures [*Chu et al*., 2011a, 2011b], suggesting a significant gap in our understanding.

[5] The University of Colorado lidar group deployed an Fe Boltzmann temperature lidar to Arrival Heights near McMurdo (77.8°S, 166.7°E) in December 2010 and has been collecting data since that time [*Chu et al*., 2011a, 2011b, 2012]. This lidar has full diurnal coverage and is capable of measuring temperatures at altitudes between 30 and 110 km. The Scott Base Medium Frequency (MF) radar is co-located with the Fe lidar at Arrival Heights. It provides continuous measurements of zonal and meridional winds from 75 to 100 km [*Baumgaertner et al*., 2005]. The simultaneous MLT temperature and wind data provide a unique opportunity for studying IGWs and their intrinsic properties at this high southern latitude. In this paper, we present a case study of two IGWs propagating over Arrival Heights simultaneously and apply filtering and hodograph analyses to determine their intrinsic properties. Our results show that these two IGWs are propagating in two different directions that are nearly perpendicular to one another.

2. Observations

[6] McMurdo and Scott Base are located on Ross Island, east of the Transantarctic Mountains. The coordinated lidar-radar observations at Arrival Heights (77.83°S, 166.67°E) are a collaboration between the United States Antarctic Program (USAP) and Antarctica New Zealand (AntNZ). The Fe Boltzmann temperature lidar consists of two independent channels probing respectively the 372 and 374 nm absorption lines of neutral Fe atoms. Temperatures can be inferred from the signal ratios between these two channels by employing the Fe Boltzmann technique [*Gelbwachs*, 1994] in the MLT region with Fe distribution. Below the Fe layer and in the region free of aerosol scattering (usually between 30 and 70 km), temperatures are derived using the Rayleigh integration technique [*Hauchecorne and Chanin*, 1980]. Principles, capabilities, and error analysis of the lidar are described in *Chu et al*. [2002], and its refurbishment and upgrade are discussed in *Wang et al*. [2012]. Plotted in Figure 1a are the temperatures measured by the Fe lidar from below 35 to 107 km over 25 h on 29–30 June 2011 at McMurdo. The lidar signal levels between 67 and 81 km are insufficient for reliable temperature derivation at required resolutions of better than 1 h, thus a data gap exists in the temperatures as shown in Figure 1. The raw lidar data (photon counts) were recorded with resolutions of 1 min and 48 m. Above this gap, the original Fe temperatures in the MLT are derived in resolutions of 0.25 h and 0.5 km, with the sampling window shifted at steps of 0.1 h and 0.1 km. The data are then temporally and vertically smoothed with a Hamming window of 0.5 h and 1 km full width at half maximum (FWHM) to further reduce the temperature errors. Therefore, waves with periods longer than 1 h and vertical wavelengths longer than 2 km are resolved. Below this gap, the Rayleigh temperatures have resolutions of 1 h and 1 km. Figure 1a shows that on the data set average, the stratopause is ~45 – 48 km and the mesopause is ~100 km.

[7] The temperature variations in Figure 1a are very large in the MLT region and are also visible in the Rayleigh temperatures above 45 km. By subtracting the dataset-mean temperatures at each altitude, the temperature perturbations are derived and shown in Figure 1b, which exceed ±30 K in the MLT region around 100 km. Both Figures 1a and 1b exhibit clear wave structures with downward phase progression from the MLT to the lower mesosphere at ~50 km, indicating that the wave(s) is upward propagating. This implies that the wave source(s) is located in the lower atmosphere. In contrast to the lidar measurements of MLT temperatures at mid to low latitudes that are commonly dominated by diurnal and semidiurnal tides [e.g., *States and Gardner*, 2000; *She et al*., 2004; *Chu et al*., 2005; *Friedman and Chu*, 2007], the temperature variations at McMurdo in Figure 1a are dominated by wave oscillations with periods of 5–8 h during the entire observation period

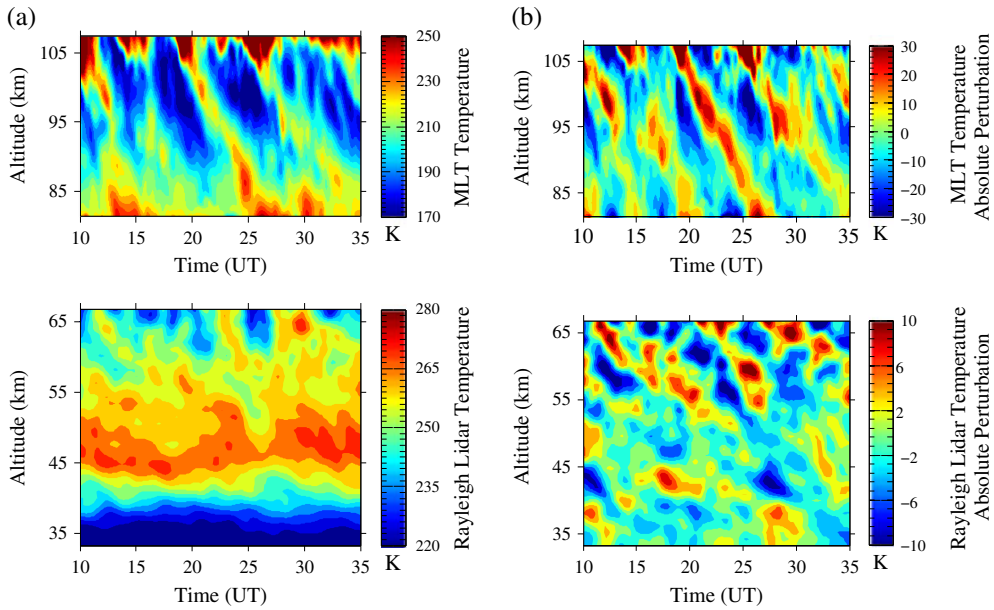

Figure 1. (a) Contours of raw temperature observations on 29–30 June 2011 at McMurdo by an Fe Boltzmann lidar in the MLT region (in the altitude range of 81–107 km) and from Rayleigh integration (in the altitude range of 33–67 km). The data gap between 67 and 81 km is due to insufficient signal levels for reliable temperature derivation at required resolutions of better than 1 h. (b) Contours of corresponding absolute temperature perturbations.

(~25 h) while diurnal or semidiurnal tides are not apparent. Such wave oscillations with periods of 5–8 h are a common feature of the MLT temperatures at McMurdo. For example, Figure 4 in *Chu et al*. [2011a] exhibits a strong wave oscillation with a period of 6.5–7 h on 28–29 January 2011, while Figure 2 in *Chu et al*. [2011b] shows a strong wave oscillation with a period of ~8 h on 28 May 2011 at McMurdo. Therefore, it is intriguing to ask what causes such large-amplitude wave oscillations. We will argue in the rest of the paper that inertia-gravity waves are the most likely mechanism.

[8] To fully characterize gravity waves, simultaneous wind data are needed. Such wind data are obtained with the Scott Base MF radar whose receiver is co-located with the Fe lidar at Arrival Heights. This radar operates at 2.9 MHz with a FWHM field of view of 30°. It has near-continuous temporal coverage and has been collecting wind data at heights between 70 and 100 km since 1982 [*Fraser*, 1984]. The peak output power of the transmitter is 60 kW and the pulse repetition frequency is 8 Hz. By using the full correlation analysis technique, zonal and meridional winds can be calculated [*Baumgaertner et al*., 2005]. Illustrated in Figure 2 are the MF radar winds in zonal and meridional directions taken simultaneously with the lidar temperature measurements on 29–30 June 2011. The MF radar uses a pulse width of 30 μs, corresponding to a fundamental vertical resolution of 4.5 km, but the data are oversampled to have the display vertical resolution of 2 km in Figure 2. The temporal resolution of the MF radar wind is 0.5 h; therefore, the MF radar can resolve waves with periods longer than 1 h and vertical wavelengths longer than 9 km. In Figure 2, we see large wind perturbations in both the zonal and meridional directions; additionally, downward phase progression is clearly seen. The perturbation periods are shorter than diurnal or semidiurnal tides, but are around 5–8 h, which is very similar to the wave periods deduced in the MLT temperatures measured by the lidar.

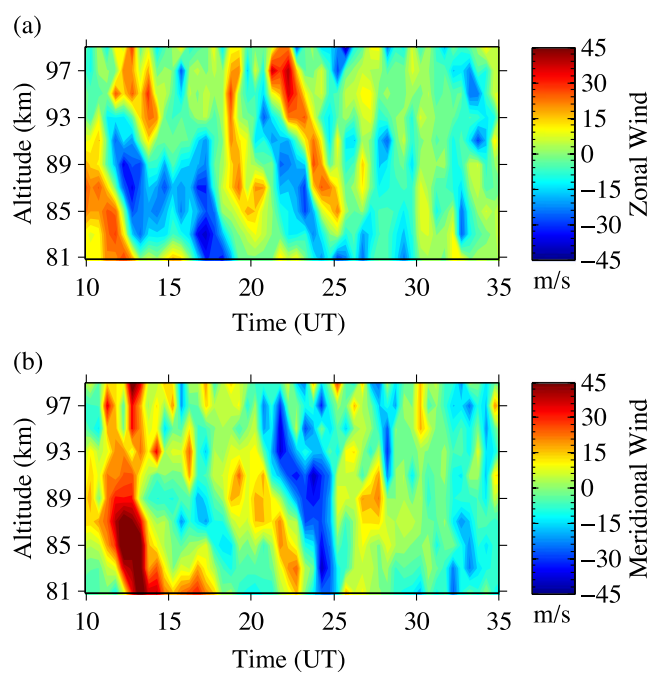

Figure 2. Contours of raw (a) zonal and (b) meridional wind observations on 29–30 June 2011 by the Scott Base MF radar in the MLT region (81–99 km). Data below 93 km may be considered reliable measurements of the neutral atmosphere wind.

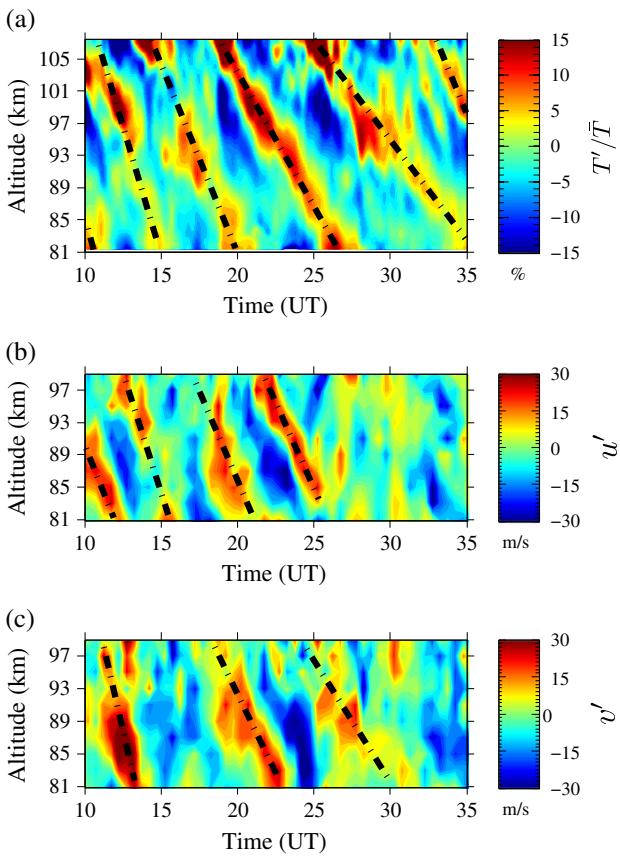

Figure 3. (a) Relative temperature perturbations (in the altitude range of 81–107 km) and (b) zonal and (c) meridional wind perturbations (81–99 km) in the MLT region on 29–30 June 2011. Diurnal and semidiurnal tides are removed from the raw perturbations. The black dash-dotted lines highlight the positive phase fronts of the waves.

[9] To combine the lidar and radar measurements for studies of the inertia-gravity waves, we derive the IGW-induced perturbations in the temperatures and winds by deriving relative temperature perturbations and absolute wind perturbations, in which the background temperatures/winds, and the perturbations induced by tides and planetary waves, are removed. Relative temperature perturbations are derived via subtracting the daily mean temperature at each altitude and then dividing by this mean. In order to minimize contamination of planetary wave oscillations, a linear trend in the time domain is removed from the original perturbations at each altitude, followed by a subtraction of a linear trend in the spatial domain as demonstrated in *Lu et al.* [2009]. To derive the wave-induced perturbations from the MF radar data, the tides are removed from the original wind observations by subtracting a temporal fitting of diurnal and semidiurnal period sinusoidal functions at each altitude. Figure 3 shows the derived wave perturbations in temperature and zonal and meridional winds, where the positive phase fronts of the waves are highlighted by black dash-dotted lines. Clear downward phase progression is observed, implying upward propagation of gravity waves. Two different periods are seen in the perturbations. The wave perturbation with a period of ~5 h dominates the zonal wind and the first half of the temperature measurements, while the amplitude of the wave perturbation with a period of ~7–8 h is stronger in the meridional wind and in the second half of the temperature measurements. Figure 3 suggests that two inertia-gravity waves may have been observed at the same time over Arrival Heights. We perform detailed analyses in the next sections to confirm this hypothesis and then derive the intrinsic properties of these two waves.

3. Wave Analysis Methodology

[10] To verify whether two IGWs are present simultaneously, detailed spectral information on the waves is determined from the fast Fourier transform (FFT) spectra for the three fields, as shown in Figure 4. Large-amplitude ~8 h period peaks are seen in the temperature spectra at all altitudes, in the zonal wind spectra at $z = 85$–89 km, and in the meridional wind spectra at $z = 83$–91 km. Distinct ~5 h period peaks are also seen in the temperature spectra at most altitudes, in the zonal wind spectra at $z = 81$–97 km, and in the meridional wind spectra but with a smaller amplitude at $z = 81$–85 km. For each of the three fields and at each altitude, if a spectral peak is found in-between periods of

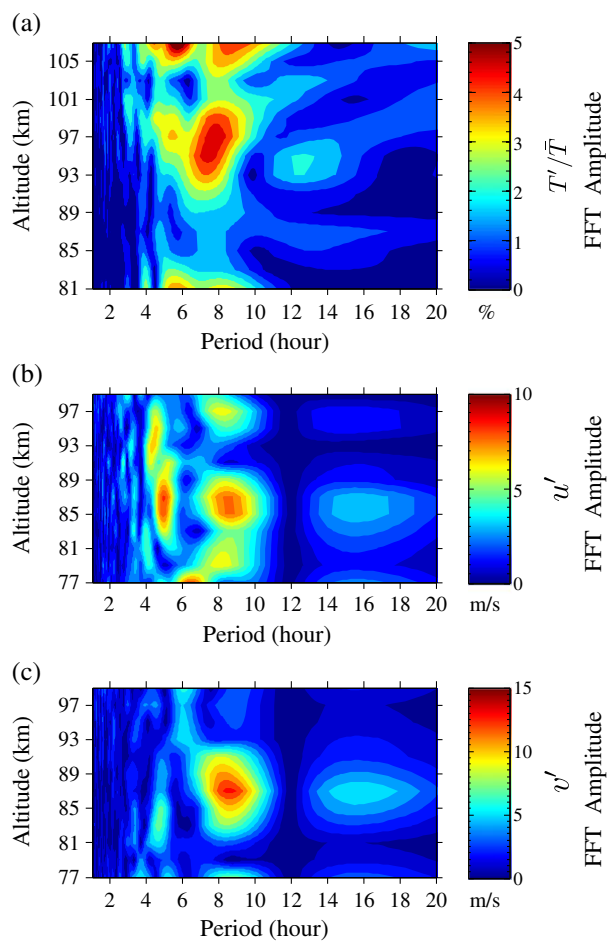

Figure 4. FFT amplitudes of (a) relative temperature perturbations (81–107 km) and (b) zonal wind and (c) meridional wind perturbations (81–99 km) in the MLT region on 29–30 June 2011.

Table 1. Observed Wave Properties for Two IGWs Derived From Temperature and Wind Fields[a]

Wave	Data Field	τ (h)	λ_z (km)	c_z (m/s)	θ (deg)	$\bar{U}_h$ (m/s)	$\frac{d\bar{U}_h}{dz}$ (10^{-4} s^{-1})
7.7 h Wave	T	7.7 ± 0.2	22 ± 2	0.8 ± 0.1	11 ± 5	2 ± 3	2 ± 1
	u	7.9 ± 0.5					
	v	7.9 ± 0.4					
5 h Wave	T	5.0 ± 0.1	23 ± 2	1.2 ± 0.1	100 ± 4	-2 ± 4	3 ± 1
	u	4.9 ± 0.1					
	v	4.8 ± 0.2					

[a]Observed period (τ), vertical wavelength (λ_z), vertical phase speed (c_z), azimuth angle of the wave horizontal propagation direction (θ), horizontal background wind speed ($\bar{U}_h$), and its vertical shear ($\frac{d\bar{U}_h}{dz}$).

4–6 or 6–10 h for one of the two waves, the period corresponding to this spectral peak is taken to represent the observed period of this wave at this altitude. The mean observed periods (τ) are obtained by averaging the results over all these altitudes; the results for both waves are summarized in all three fields in Table 1. In order to determine the errors in the period analysis, a nonlinear least square fitting is applied to the time series using a sum-of-two-sine model; this is performed at each altitude and for each field of data. The model is written as follows:

$$x(t) = A\cos\left(\frac{2\pi}{\tau_1}t + \varphi_1\right) + B\cos\left(\frac{2\pi}{\tau_2}t + \varphi_2\right) \quad (1)$$

[11] where $x(t)$ represents the time series of the perturbation; A, τ_1, and φ_1 are the amplitude, apparent period, and phase for the first wave; while B, τ_2, and φ_2 are the parameters for the second wave. The results of the fitted periods in the two sine functions (not shown here) are in accordance with the results obtained from the FFT analysis. The errors of the periods are then determined from the 95% confidence levels of the fitted periods at each altitude. The mean values of these errors for each wave are given in Table 1 and are used later in this paper to estimate the errors in the intrinsic periods and other wave properties derived from the gravity wave dispersion and polarization relations. Since the temperatures have better temporal resolutions and smaller errors, the periods derived from the temperature data are taken as the observed periods of the waves. Hereinafter, whenever the information of observed period or its error is needed, we use the values derived from the temperatures. These two waves are referred to as 7.7 h wave and 5 h wave, respectively.

[12] The two isolated spectral peaks shown in Figure 4 could be an indication of two independent waves propagating across the lidar/radar fields of view at the same time. Or it could be due to a single wave that is Doppler shifted from one period to another over time. To examine this, we use wavelet analysis that provides information about the time when each wave is present in the spectra. The Morlet wavelet spectra for each data field at two example altitudes of 85 and 87 km are shown in Figure 5. The cone of influence (COI) is denoted by the white dashed lines, outside of which is the region in the spectrum where the true peak magnitude is reduced and a false peak might appear [*Torrence and Compo*, 1998]. White crosses on the contours denote the local peak between the periods of 4 and 10 h. Both the zonal and meridional wind wavelet spectra clearly show the 5 h wave and the 7.7 h wave present at the same time regardless of their locations relative to the COI. This confirms that two independent waves were in the wind field at the same time. In the temperature wavelet spectrum, these two waves are clearly seen at the same time at 87 km. At 85 km, however, the two peaks almost merge together below the COI from 20 to ~25 UT. Although two peaks are present above the COI at other times, they are subject to edge effects and thus must be interpreted with care. We will come back to this issue after separating the two waves and investigating their intrinsic properties in section 4.

3.1. Band-Pass Filtering to Separate Two Waves

[13] To separate these two waves, all three fields are band-pass filtered by a sixth-order Butterworth filter with passbands at 6–10 and 3.5–5.5 h for the 7.7 h wave and 5 h wave, respectively. The choice of the cutoff frequencies is a tradeoff between minimizing the interference from the other wave and ensuring that the desired wave is not attenuated too severely. Since the 7.7 h wave is generally stronger, its final results are not very sensitive to the choice of its cutoff frequency; thus, the passband of 6–10 h is a good compromise such that little energy is lost. In contrast, the 5 h wave suffers spectral leakage from the 7.7 h wave (which has the larger amplitude). For this wave, a passband of 3.5–5.5 h greatly reduces the spectral leakage from the 7.7 h wave, but does not severely attenuate the 5 h wave. Figure 6 shows the results for the passband of 6–10 h, and Figure 7 shows the results for the passband of 3.5–5.5 h. The filtered data for each field display clear downward phase progressions. Additionally, both waves are quasi-monochromatic. It is apparent in Figures 6 and 7 that the filtered 7.7 h and 5 h waves have larger or smaller amplitudes simultaneously in the wind field, which will not be the case if a single wave is Doppler shifted from one period to another. It is also noted that Figures 6 and 7 show clear wave structures in the zonal and meridional winds after 30 UT, even though the amplitudes of both waves become smaller; however, the original wind perturbations (Figure 3) do not show such clear wave signatures. By reconstructing time series from these two filtered perturbations only and comparing them with the raw wind fields, we find that this phenomenon is caused by the destructive interference of these two waves after 30 UT. The results of Figures 6 and 7 support our hypothesis that two independent waves were propagating across our observational field of view simultaneously.

[14] The vertical wavelength (λ_z) of each wave is then determined from the filtered temperature data because of its higher vertical resolution and larger altitude coverage than the wind data. A linear least square fit is first performed to the phase lines of the filtered temperature data to obtain

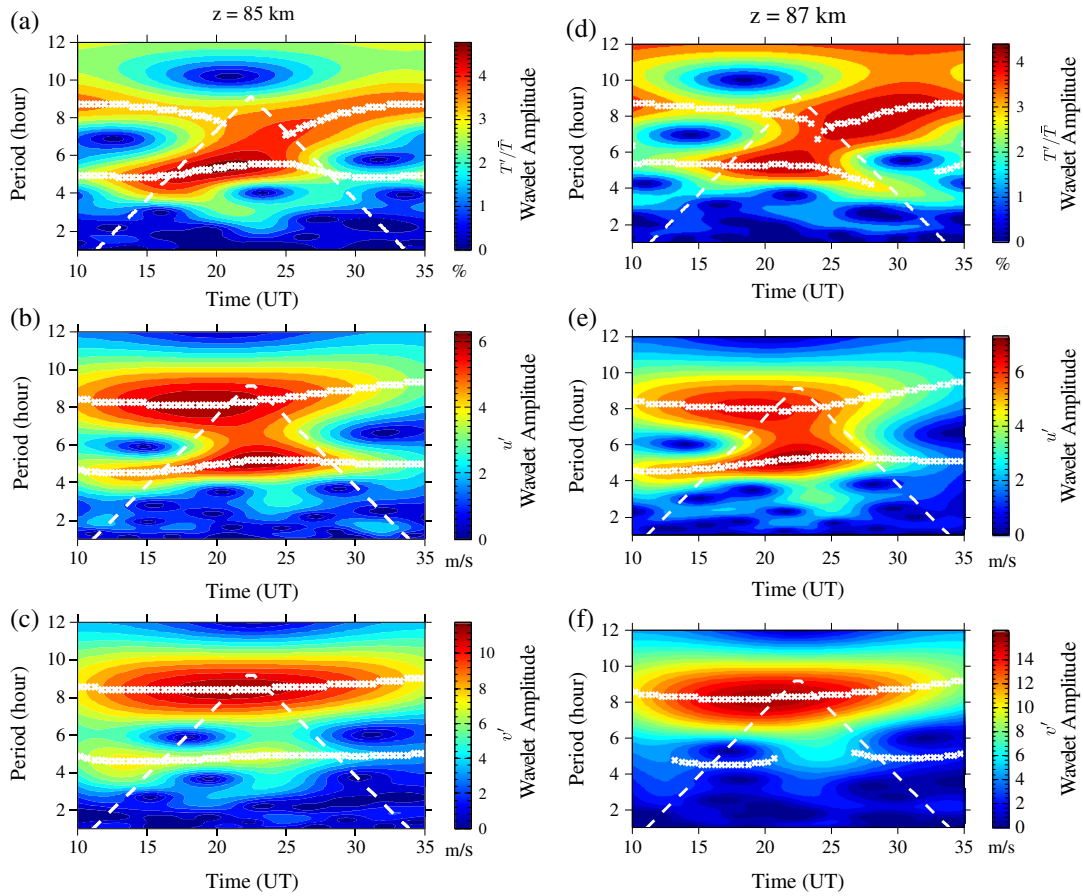

Figure 5. Amplitudes of the Morlet wavelet spectra at 85 km and 87 km for (a and d) relative temperature perturbations and (b and e) zonal and (c and f) meridional wind perturbations on 29–30 June 2011. The white crosses denote the local maximum power in the wavelet spectra with periods between 4 and 10 h. The white dashed line in each contour denotes the cone of influence (COI) for the wavelet analysis.

the derivative of the altitude of the phase line with respect to time, i.e., the vertical phase speed (c_z). The vertical wavelength λ_z is then calculated by multiplying c_z with the observed period (τ). We obtain $\lambda_z = 22 \pm 2$ km for the 7.7 h wave and $\lambda_z = 23 \pm 2$ km for the 5 h wave. The uncertainties in λ_z and c_z are determined from the 95% confidence levels of the fittings. The values and errors of λ_z and c_z are listed in Table 1. These results are generally comparable with the long-period oscillations observed by *Collins et al.* [1994] in the bottomside of the Na layer at the South Pole. They observed large-amplitude oscillations with periods around 5–12 h with a Na lidar. Their derived vertical wavelengths are close to 22 km for wave periods of 5 h, but are shorter (12–18 km) for periods of 7–8 h. Note that the IGW observed by *Nicolls et al.* [2010] in the Arctic had a long period of ~10.5 h and a short vertical wavelength of ~4–10 km.

3.2. Hodographs for Determining Wave Propagation Directions

[15] We now treat each filtered wave as a quasi-monochromatic wave and determine its propagation direction from a hodograph analysis. Hodograph analyses of wind data have been applied in altitude to study the intrinsic properties of gravity waves in the MLT [e.g., *Hu et al.*, 2002; *Li et al.*, 2007; *Lu et al.*, 2009, *Nicolls et al.*, 2010]. In this study, we choose to make temporal hodograph analyses of the MF radar wind. First, we do this because the overlapping range between the lidar and radar observations (less than 20 km between 80 and 100 km) is shorter than the vertical wavelengths of the waves (i.e., 22–23 km from the previous section). This is insufficient to accurately resolve the observed IGWs. Second, the vertical resolution (4.5 km) of the radar wind is too coarse to determine the orientation of the hodograph ellipse accurately. In contrast, the overlapping time between the lidar and radar observations is long (~25 h), so sufficient data are available to make the hodographs in the temporal domain. From a theoretical standpoint, hodograph analyses in the temporal or altitudinal domains are equivalent for a monochromatic wave in a constant background wind and temperature, in terms of determining the wave parameters (such as horizontal propagation direction).

[16] The hodograph analysis is based on the IGW polarization relation [e.g., *Tsuda et al.*, 1990; *Nakamura et al.*, 1993]:

$$\tilde{U}_{\parallel} = i\frac{\hat{\omega}}{f}\tilde{U}_{\perp} \tag{2}$$

where $\tilde{U}_{\parallel}$ and $\tilde{U}_{\perp}$ are the complex representations of the horizontal wind perturbations parallel and perpendicular to the wave horizontal propagation direction, respectively,

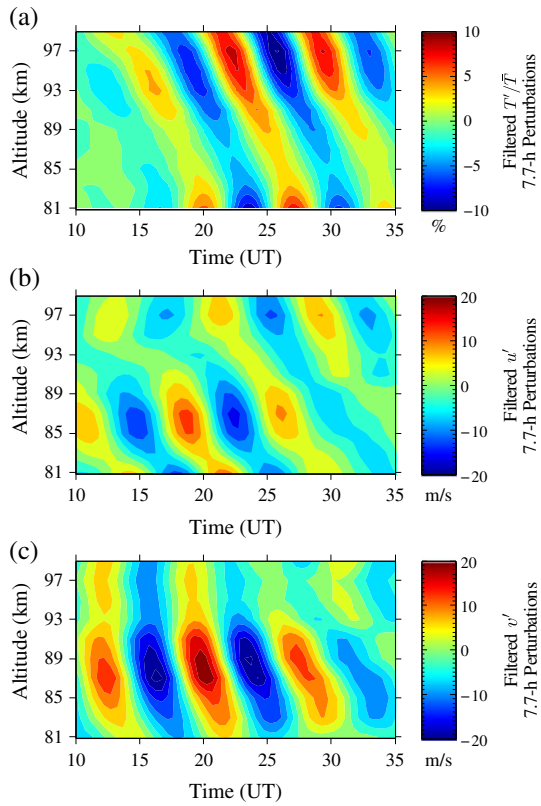

Figure 6. (a) Relative temperature perturbations and (b) zonal and (c) meridional wind perturbations filtered by a sixth-order band-pass Butterworth filter with lower and upper cutoff frequencies at 1/10 and 1/6 h^{-1}, respectively.

$\hat{\omega}$ is the intrinsic frequency of the wave, and f is the Coriolis parameter. At McMurdo (77.8°S), the inertial period is $2\pi/f = 12.24$ h. In deriving equation (2), we assume that the perturbations are induced by a monochromatic wave, and thus $\tilde{U}_{\parallel}$ and $\tilde{U}_{\perp}$ are written as follows:

$$\tilde{U}_{\parallel} = \left|\tilde{U}_{\parallel}\right| \exp\left[\mathrm{i}\left(k_h x_h + mz - \omega t - \Phi_{\tilde{U}_{\parallel}}\right) + \frac{z}{2H}\right] \quad (3)$$

$$\tilde{U}_{\perp} = \left|\tilde{U}_{\perp}\right| \exp\left[\mathrm{i}\left(k_h x_h + mz - \omega t - \Phi_{\tilde{U}_{\perp}}\right) + \frac{z}{2H}\right] \quad (4)$$

respectively. Here k_h and x_h are the horizontal wave number and distance, respectively; m is the vertical wave number and it is negative in the case of downward phase progression; ω is the observed (i.e., ground-based) frequency; $H = R\bar{T}/g$ is the density-scale height, calculated from the observed mean temperature $\bar{T}$, the gas constant of dry air R, and the gravitational acceleration g; $\Phi_{U_{\parallel}}$ and $\Phi_{U_{\perp}}$ are the initial phases of $\tilde{U}_{\parallel}$ and $\tilde{U}_{\perp}$, respectively. Equation (2) neglects background shear terms [e.g., *Fritts and Alexander*, 2003]. This is applicable in our case, because such shear terms (calculated from the background wind) are sufficiently small (see Table 1). Equation (2) is also derived under the Boussinesq approximation, which assumes that the wave phase speed is much less than the sound speed and that $\lambda_z \ll 4\pi H$ [*Kundu*, 1990]. According to equation (2), the gravity-wave-induced $\tilde{U}_{\parallel}$ and $\tilde{U}_{\perp}$ exhibit elliptical or circular polarization. The major axes of the ellipses point in the direction of wave propagation, although with a 180° ambiguity.

[17] This 180° ambiguity in the propagation direction is resolved by making use of the lidar temperature data. We derive the polarization relation between the relative temperature perturbation $\tilde{T}$ and $\tilde{U}_{\parallel}$ for an IGW with $N \gg \hat{\omega}$:

$$\tilde{T} = \frac{1}{g}\left(\mathrm{i}m + \frac{1}{2H}\right)\frac{\hat{\omega}^2 - f^2}{\hat{\omega}\, k_h}\tilde{\mathrm{U}}_{\parallel} \quad (5)$$

where $\tilde{T}$ is the complex representation of the relative temperature perturbation $T'/\bar{T}$ given by

$$\tilde{T} = \left|\tilde{T}\right| \exp\left[\mathrm{i}\left(k_h x_h + mz - \omega t - \Phi_{\tilde{T}}\right) + \frac{z}{2H}\right] \quad (6)$$

[18] Here, $\Phi_{\tilde{T}}$ is the initial phase of $\tilde{T}$. Equation (5) agrees with *Vadas* [2012, equations (B8), (B9), and (B11)]. The derivation of equation (5) assumes that H and the background winds are constant in time and in the horizontal plane, but can vary slowly in altitude. The phase relation between $\tilde{T}$ and $\tilde{U}_{\parallel}$ can be derived from equation (5) as

$$\Phi_{\tilde{U}_{\parallel}} - \Phi_{\tilde{T}} = \arctan(m \cdot 2H) \quad (7)$$

[19] Equation (7) poses a constraint on the wave propagation direction; only when $\tilde{U}_{\parallel}$ is along the correct propagation direction of the wave, is $\Phi_{\tilde{U}_{\parallel}} - \Phi_{\tilde{T}}$ (extracted from the wind

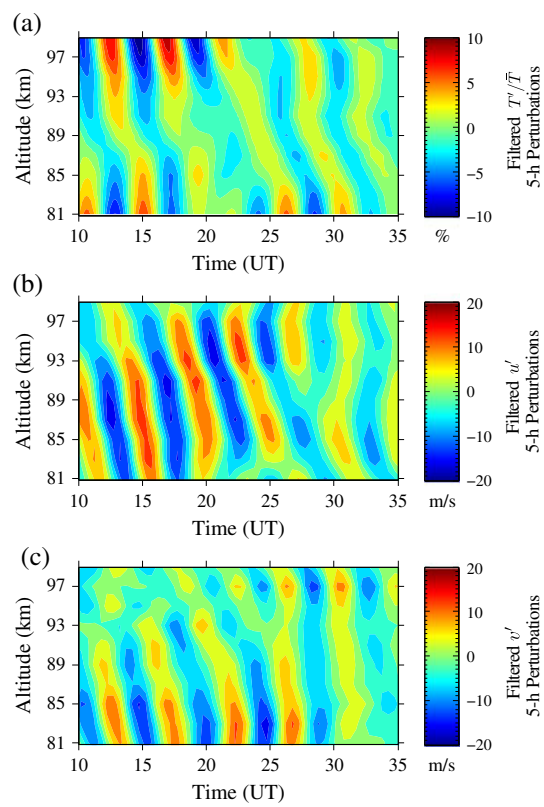

Figure 7. (a) Relative temperature perturbations and (b) zonal and (c) meridional wind perturbations filtered by a sixth-order band-pass Butterworth filter with lower and upper cutoff frequencies at 1/5.5 and 1/3.5 h^{-1}, respectively.

and temperature observations) close to $\arctan(m \cdot 2H)$. The opposite direction of the wave leads to $\Phi_{\tilde{U}_\parallel} - \Phi_{\tilde{T}}$ approaching $\arctan(m \cdot 2H) \pm 180°$. Therefore, this extra constraint helps remove the 180° ambiguity.

[20] The actual $\Phi_{\tilde{U}_\parallel} - \Phi_{\tilde{T}}$ are derived from the temperature and wind perturbations, in which we first project the zonal and meridional wind perturbations to one of the two directions along the major axis inferred from the hodograph analyses and derive the corresponding horizontal wind perturbations ($U_\parallel{}'$). Then, $\Phi_{\tilde{U}_\parallel}$ and $\Phi_{\tilde{T}}$ are extracted by performing a nonlinear least square fitting to the wind and temperature perturbations using the real part of the monochromatic wave models as shown in equations (3) and (6). We then compare the derived $\Phi_{\tilde{U}_\parallel} - \Phi_{\tilde{T}}$ to $\arctan(m \cdot 2H)$. If $\Phi_{\tilde{U}_\parallel} - \Phi_{\tilde{T}}$ is close to $\arctan(m \cdot 2H)$, then the direction we chose is correct; otherwise, if $\Phi_{\tilde{U}_\parallel} - \Phi_{\tilde{T}}$ is close to $\arctan(m \cdot 2H) \pm 180°$, then the correct direction is 180° opposite to the originally chosen direction. Thus, combining the wind and temperature data allows us to unambiguously identify the propagation directions from hodographs.

3.3. Derivations of Wave Intrinsic Properties

[21] The absolute value of the intrinsic frequency $\hat{\omega}$ can be calculated from the amplitude ratio between $\tilde{U}_\parallel$ and $\tilde{U}_\perp$ using equation (2). This has been a common approach used to derive the intrinsic properties of IGWs [e.g., *Hu et al.*, 2002; *Lu et al.*, 2009]. For the 7.7 h wave, we find that the amplitude ratios of the fitted ellipses vary dramatically with altitude (in the range of 1.2–3.3, giving an estimate of an intrinsic period of 3.5–10 h from equation (2)); however, the major axes of these ellipses are oriented similarly. If we use this method to determine the intrinsic periods directly, large errors result. This likely occurs because there are two IGWs; although the filtering works well, some spectral leakage occurs and appears to greatly impact the amplitudes of the wind perturbations (and thus the ratios). Therefore, we take a different approach instead. Since the horizontal wave propagation direction has been unambiguously determined, and the apparent period and background winds are known, the intrinsic properties can be determined from the gravity wave dispersion relation and the definition of the intrinsic frequency [*Fritts and Alexander*, 2003]:

$$k_h{}^2 = \frac{\hat{\omega}^2 - f^2}{N^2}\left(m^2 + \frac{1}{4H^2}\right) \tag{8}$$

$$\hat{\omega} = \omega - k_h \bar{U}_h \tag{9}$$

where N is the buoyancy frequency computed from the dataset-mean lidar temperature profile $\bar{T}(z)$ as $N = \sqrt{\frac{g}{\bar{T}(z)}\left(\frac{\partial \bar{T}(z)}{\partial z} + \frac{g}{C_p}\right)}$. Note that equation (8) is a simplified form of equation (24) in *Fritts and Alexander* [2003], where we have used the fact that $N \gg \hat{\omega}$ for IGWs. In deriving equation (8), it is also assumed that N is constant in x, y, and t, but varies slowly in z. Additionally, we assume that the speed of sound c_s is much larger than the wave horizontal phase speed (i.e., the Boussinesq approximation) [*Kundu*, 1990]. From equation (9), we have $k_h = (\omega - \hat{\omega})/\bar{U}_h$. Substituting k_h in equation (8) with this new expression, we obtain the following quadratic equations for $\hat{\omega}$:

$$\left(\frac{N^2}{\bar{U}_h{}^2} - m^2 - \frac{1}{4H^2}\right)\hat{\omega}^2 - \frac{2N^2\omega}{\bar{U}_h{}^2}\hat{\omega} + f^2\left(m^2 + \frac{1}{4H^2}\right) + \frac{N^2\omega^2}{\bar{U}_h{}^2} = 0 \tag{10}$$

[22] Solving equation (10), we obtain the following solutions for $\hat{\omega}$:

$$\hat{\omega} = \frac{\frac{N^2\omega}{m^2+\frac{1}{4H^2}} \pm \sqrt{\left(\frac{N^2\omega}{m^2+\frac{1}{4H^2}}\right)^2 - \left(\frac{N^2}{m^2+\frac{1}{4H^2}} - \bar{U}_h{}^2\right)\left(\frac{N^2\omega^2}{m^2+\frac{1}{4H^2}} + f^2\bar{U}_h{}^2\right)}}{\frac{N^2}{m^2+\frac{1}{4H^2}} - \bar{U}_h{}^2} \tag{11}$$

The corresponding solutions for k_h are

$$k_h = \frac{-\omega\bar{U}_h \mp \frac{\bar{U}_h}{|\bar{U}_h|}\sqrt{(\omega\bar{U}_h)^2 + \left(\frac{N^2}{m^2+\frac{1}{4H^2}} - \bar{U}_h{}^2\right)(\omega^2 - f^2)}}{\frac{N^2}{m^2+\frac{1}{4H^2}} - \bar{U}_h{}^2} \tag{12}$$

[23] These expressions are similar to those used by *Liu and Meriwether* [2004] and *Li et al.* [2007]. The intrinsic horizontal and vertical group velocities of the wave packet describe the energy propagation and they are derived by taking partial derivatives with respect to k_h and m on both sides of equation (8) [e.g., *Fritts and Alexander*, 2003]:

$$c_{gh} = \frac{\partial\hat{\omega}}{\partial k_h} = \frac{k_h(N^2 - \hat{\omega}^2)}{\hat{\omega}\left(k_h{}^2 + m^2 + \frac{1}{4H^2}\right)} \tag{13}$$

$$c_{gz} = \frac{\partial\hat{\omega}}{\partial m} = -\frac{m(\hat{\omega}^2 - f^2)}{\hat{\omega}\left(k_h{}^2 + m^2 + \frac{1}{4H^2}\right)} \tag{14}$$

[24] We will utilize equations (11)–(14) to estimate the intrinsic properties of each wave.

4. Wave Analysis Results

4.1. The 7.7 h Inertia-Gravity Wave

[25] As mentioned in section 3.1, band-pass filters are used to extract two quasi-monochromatic waves. We plot the filtered zonal and meridional wind perturbations of the 7.7 h wave as hodographs in Figure 8a. Each plot in Figure 8a shows the hodograph for a given altitude between 83 and 91 km over the time range from 10 UT to 30 UT. These particular temporal and spatial ranges are chosen to coincide with when and where the wave amplitudes are large in the wind data and have the highest signal-to-noise ratio. The start and end times are denoted by stars and triangles, respectively. All five hodographs show an anticlockwise rotation in time. A least mean square (LMS) ellipse fitting is performed on each hodograph and is indicated by the

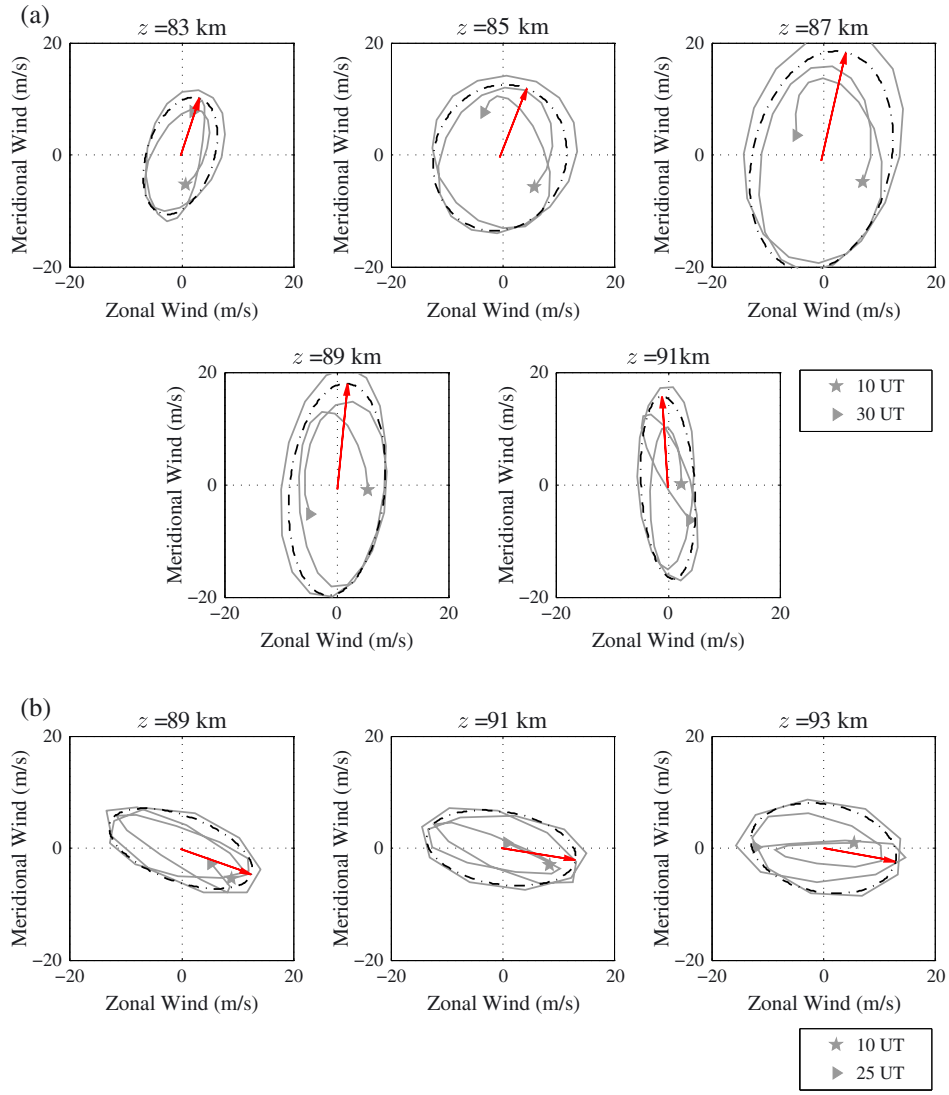

Figure 8. Temporal hodographs of zonal and meridional wind perturbations for the (a) 7.7 h wave in the altitude range of 83–91 km and for the (b) 5 h wave in the altitude range of 89–93 km. Stars and triangles denote the start and the end times, respectively. The dash-dotted ellipse on each plot shows the LMS elliptical fit of the hodograph. Red arrow is plotted along the major axis of each fitted ellipse, indicating the propagation direction of the wave.

dash-dotted ellipse. All of the ellipses are primarily elongated in the meridional direction with a slight variation in the major axis between the different altitudes. A red arrow is plotted along the major axis of each fitted ellipse, indicating a possible propagation direction of the wave, but with a 180° ambiguity.

[26] To resolve the 180° ambiguity for the 7.7 h gravity wave, we first assume that the wave propagates in the direction indicated by the red arrow in each hodograph in Figure 8a. Then we project the zonal and meridional wind perturbations along this direction and derive the corresponding horizontal wind perturbations ($U_{\parallel}'$). After that, band-pass filtered perturbations $U_{\parallel}'$ and $T'/\bar{T}$ are fitted to the real part of the monochromatic wave models (see equations (3) and (6)). The deduced phase differences $\Phi_{\tilde{U}_{\parallel}} - \Phi_{\tilde{T}}$ are shown in Figure 9a as red crosses for the altitudes from 83 to 91 km. The theoretical value ($\arctan(m \cdot 2H)$) is shown as the solid vertical line, which in this case is $286 \pm 0.7°$. The dashed vertical line shows the value of $\arctan(m \cdot 2H) - 180°$. The uncertainties caused by errors in obtaining the phase information, deriving the ellipse orientation, and determining the wave period (with temporal variation), are estimated to be $\pm 40°$ at the 95% confidence level (denoted by grey error bars). The discrepancies between the crosses and the solid vertical line mostly fall within the error bars (except at 91 km), implying that the orientation indicated by the red arrows is the correct propagation direction of this wave. Thus, we conclude that the 7.7 h wave is propagating slightly east of north at the azimuth angle of $11° \pm 5°$. Note that the larger biases seen at 91 km may be caused by spectral leakage from the shorter-period wave, because that is the altitude where the 7.7 h wave amplitude is smallest relative to the 5 h wave (see Figure 4). Therefore, we find that the hodograph method works well at those altitudes where spectral leakage from another significant wave is minimal; we also find this to be true for the 5 h wave, as discussed later.

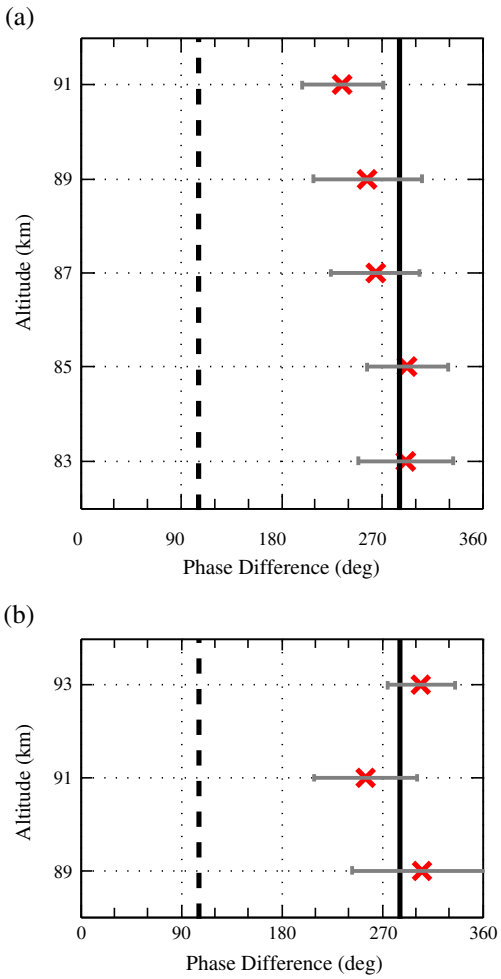

Figure 9. The deduced phase differences between $\widetilde{U}_{||}$ and $\widetilde{T}$ (red crosses) for (a) the 7.7 h wave and (b) the 5 h wave. The solid vertical line identifies the value of $\arctan(m \cdot 2H) \sim 286°$, while the dashed vertical line shows the value of $\arctan(m \cdot 2H) - 180° \sim 106°$. The grey horizontal bars denote the errors at the 95% confidence level.

[27] To calculate the intrinsic wave properties from equations (9) and (10), we need to compute $\bar{U}_h$. We first low-pass filter the zonal and meridional winds to remove variations with periods shorter than or close to the wave being examined. The sixth-order Butterworth filters with a cutoff period of 7 h for the 5 h wave and of 10 h for the 7.7 h wave are used. The horizontal background winds along each wave's propagation direction are then determined by projecting the background winds onto the coordinate system that has been rotated to be along the wave's propagation direction. $\bar{U}_h$ is then calculated as the dataset mean of the horizontal background winds at each altitude. The error of $\bar{U}_h$, $\Delta\bar{U}_h$, is calculated from the standard deviation of the horizontal background winds at each altitude. The mean values of $\bar{U}_h$ and $\Delta\bar{U}_h$ are given in Table 1. Notably, the mean background winds $\bar{U}_h$ are small for both waves, and their absolute values are ~2 m/s.

[28] There are two pairs of solutions for $\hat{\omega}$ and k_h (see equations (11) and (12)). For the current case when the denominators of the right-hand side of equations (11) and (12) are positive, i.e., $|\bar{U}_h| < U_{\lim} = N/\sqrt{m^2 + \frac{1}{4H^2}}$, there exist two positive roots for $\hat{\omega}$ and one positive and one negative roots for k_h. Positive k_h means that the wave is propagating in the positive x direction of our reference frame. We retain the pair of solutions for $k_h > 0$, because the horizontal axes of the ground-based reference frame have been rotated toward the wave propagation direction determined from the hodograph analysis. The resulting intrinsic period $\tau_I = 2\pi/\hat{\omega}$ and horizontal wavelength $\lambda_h = 2\pi/k_h$ of the 7.7 h wave are shown in Figure 10a. We find the average values of $\tau_I \sim 7.9$ h and $\lambda_h \sim 2.2 \times 10^3$ km. The intrinsic frequency is red shifted relative to the observed frequency; however, because the horizontal wavelength is large, the frequency shift is relatively small. The derived horizontal group velocity c_{gh} profile in Figure 10a has a mean of ~48 m/s, while the vertical group velocity c_{gz} has an average value of ~0.46 m/s, i.e., ~40 km/d in the vertical direction. The elevation angle of the wave propagation direction is calculated from the ratio of the vertical and horizontal group velocities and is found to be very shallow: ~0.6° from the horizon. Profiles of other properties of the 7.7 h wave, such as the intrinsic horizontal phase speed (c_{Ih}) and azimuth angle of propagation direction, are also shown in Figure 10a.

[29] It is important to derive the errors of these intrinsic parameters using the error propagation law. The three major error sources are the uncertainties in the three observed variables: ω, m, and $\bar{U}_h$. The error of each intrinsic parameter is obtained via taking derivatives of each intrinsic variable with respect to ω, m, and $\bar{U}_h$, following the method developed by Chu in *Chu and Papen* [2005] and in *Wang et al.* [2010] for lidar temperature and wind error analysis (see their equations (19) and (20)). Taking $\hat{\omega}$ as an example, its errors are derived as

$$\Delta\hat{\omega} = \frac{\partial\hat{\omega}}{\partial\omega}\Delta\omega + \frac{\partial\hat{\omega}}{\partial m}\Delta m + \frac{\partial\hat{\omega}}{\partial\bar{U}_h}\Delta\bar{U}_h \tag{15}$$

[30] Because the three error terms of ω, m, and $\bar{U}_h$ are not correlated, the final error is given by the square root of the sum of the squares of each derivative term. In the example of $\hat{\omega}$, the final error is given by

$$(\Delta\hat{\omega})_{rms} = \sqrt{\left(\frac{\partial\hat{\omega}}{\partial\omega}\Delta\omega\right)^2 + \left(\frac{\partial\hat{\omega}}{\partial m}\Delta m\right)^2 + \left(\frac{\partial\hat{\omega}}{\partial\bar{U}_h}\Delta\bar{U}_h\right)^2} \tag{16}$$

[31] Similar error propagation equations are used for all of the intrinsic parameters we determine. Two approaches can be used to calculate the terms in equation (16). One is to take numerical derivatives, and the other is to employ a Monte Carlo method. For the latter, we compute the wave properties from equations (11)–(14) with varied input variables of $\bar{U}_h$, ω, and m. The computation is done with a three-loop iteration. For each loop, each variable takes 10 evenly spaced values from the mean ω, m, and $\bar{U}_h$ minus their errors to the means plus their errors. The final uncertainty for each calculated wave parameter is then determined by the standard deviation of all the solutions in the iteration process. We have tried both approaches and obtained comparable results for each intrinsic parameter. The error bars derived from the Monte Carlo method are plotted in Figure 10a.

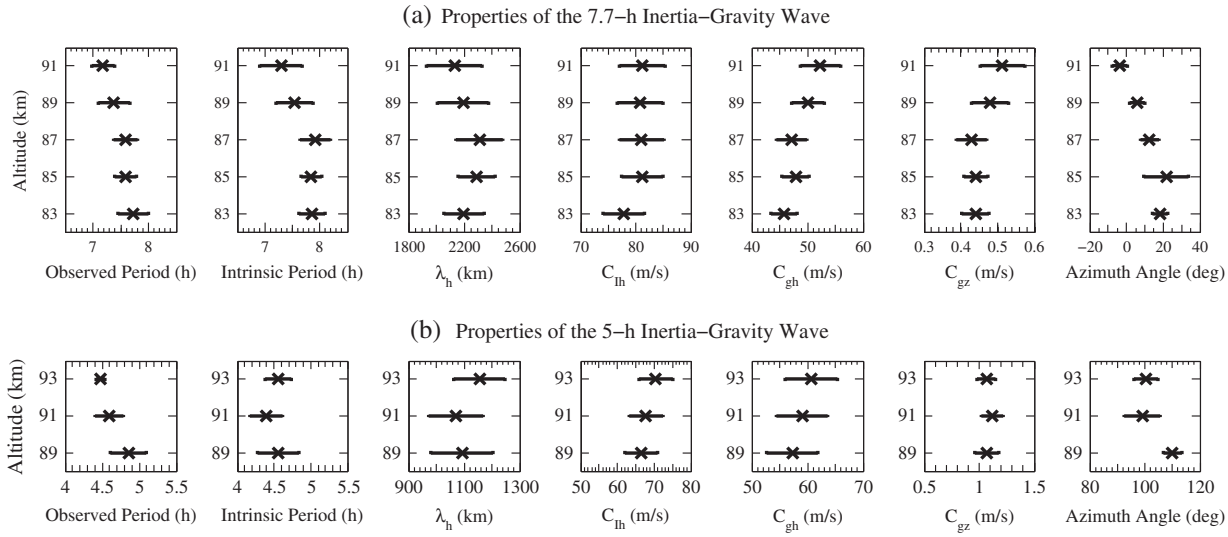

Figure 10. Wave properties (crosses) and corresponding errors (horizontal bars) for (a) the 7.7 h wave and (b) the 5 h wave. From left to right, the properties are observed period, intrinsic period, horizontal wavelength (λ_h), horizontal intrinsic phase speed (C_{Ih}), horizontal group velocity (C_{gh}), vertical group velocity (C_{gz}), and azimuth angle of the wave horizontal propagation direction.

4.2. The 5 h Inertia-Gravity Wave

[32] We investigate the intrinsic properties for the 5 h wave using the same procedure as the 7.7 h wave. The temporal hodographs for this wave are shown in Figure 8b for 89–93 km between 10 UT and 25 UT. Strong leakage from the 7.7 h wave at altitudes from 83 to 89 km (see Figure 4) makes it hard to obtain reliable results outside the limited spatial range of 89–93 km. Shown in Figure 9b are the calculated phase differences between the temperature and horizontal wind perturbations for $z = 89$, 91, and 93 km. The derived phase differences are close to the theoretical value. Therefore, we conclude that this wave propagates primarily from west to east with an average propagation azimuth angle of $100° \pm 4°$ east of north, as illustrated by the red arrows in Figure 8b. The intrinsic properties for the 5 h wave are shown in Figure 10b. Notably, the average $\tau_I \sim 4.5$ h, which is blue shifted relative to the observed periods, and the average $\lambda_h \sim 1.1 \times 10^3$ km. For this 5 h wave, the mean c_{gh} is calculated to be ~58 m/s, and c_{gz} is ~1.1 m/s, i.e., 95 km/d in the vertical direction. The elevation angle of this wave is determined to be ~1.1° from the horizon.

[33] The results from the hodograph analysis support our hypothesis that there are two independent IGWs observed in the temperature and wind perturbations, because these two filtered waves were found to propagate in two different directions that are nearly perpendicular to each other. This is different from an alternate hypothesis that an IGW source can excite waves with different parameters that arrive at the observation altitude at different times; in this case, a single wave's period would steadily shift from one period to another over the 30 h observation window. Furthermore, the 5 h wave propagates at a steeper elevation angle than the 7.7 h wave, which means that the 5 h wave has a greater ability to induce vertical motions (and thus temperature oscillations) than the 7.7 h wave. This explains why the dominant periods in the temperature wavelet spectrum appear to transition from 5 to 8 h in Figure 5. Since in the first half of the measurement the amplitude of the 5 h wave is comparable to that of the 7.7 h wave, the 5 h wave induces larger temperature oscillations than the 7.7 h wave. Thus, it would dominate the temperature wavelet spectrum in the first half of Figure 5. But as the 5 h wave amplitude reduces more quickly than the 7.7 h wave in the second half of the measurement (due, perhaps, to source changes in time), the 7.7 h wave would dominate the temperature spectrum during the second half of the measurement (see Figure 5).

5. Discussion

[34] Although both waves are treated as IGWs in this paper, the 7.7 h and 5 h wave periods are close to that of the terdiurnal (8 h) tide and 4.8 h tide. However, the 7.7 h wave in our study is unlikely to be a terdiurnal tide for the following reasons. First, the vertical wavelengths of terdiurnal tides are generally much larger than that computed for the 7.7 h wave in our case. *Du and Ward* [2010] investigated the global structure of the terdiurnal tide, including migrating and 10 nonmigrating components, using the extended Canadian Middle Atmosphere Model. Their study shows the vertical phase profile of the total terdiurnal tide superposed from the 11 components in June at 60°S, 130°E [*Du and Ward*, 2010, Figure 6b], from which the vertical wavelength is inferred to be ~65 km, a factor of 3 greater than the observed value in our study. Model simulations of the migrating terdiurnal tide performed by *Smith and Ortland* [2001] also support this point, since they indicate that the shortest vertical wavelength for all of the modes is 47 km, nearly twice as large as that in the current observation. Second, as shown in Figure 10, we observed large variations of the dominant periods with altitude, which do not satisfy the definition of a tidal wave, i.e., a harmonic of the Earth's rotation period. A notable feature of each

wave is that the observed wave period decreases with increasing altitude. In Figure 10, the observed period of 7.7 h wave decreases from $\tau_1 = 7.7 \pm 0.3$ h at $z = 83$ km to $\tau_1 = 7.2 \pm 0.2$ h at $z = 91$ km, and the 5 h wave period decreases from $\tau_2 = 4.9 \pm 0.2$ h at $z = 89$ km to $\tau_2 = 4.5 \pm 0.1$ h at $z = 93$ km. According to *Nicolls et al.* [2010], such a feature can be explained by a spectrum of IGWs generated by a geostrophic adjustment of the jet stream. However, we note that these variations may be within our error bars. Third, modeling work by *Du and Ward* [2010] shows that the largest amplitude of the terdiurnal tides is given by the migrating component. Examination of wind and temperature data from the Modern Era Retrospective-Analysis for Research and Applications (MERRA) reanalysis at the highest-pressure level (0.1 hPa, ~59 km) shows no evidence of a significant zonal wave number 3 pattern; this is also suggestive that the terdiurnal tide cannot explain the current observations.

[35] Both the background temperature and winds play a role in wave propagation through the atmosphere, the latter typically being much more important in allowing (or disallowing) the gravity wave propagation. Unfortunately, the lack of extensive middle atmospheric wind and temperature measurements up to the MLT prohibits detailed studies involving ray tracing such slow waves through realistic atmosphere [e.g., *Nielsen et al.*, 2012]. Such work is therefore outside the scope of this study. We now roughly identify the sources of the observed IGWs by making a number of simple assumptions. For both waves, the vertical group velocities (calculated above) are significantly slower than the horizontal group velocities. This implies that it would take ~1–2 days for each wave to propagate to the MLT (assuming that the vertical wind is negligible). Assuming that the horizontal background wind along the wave propagation path is also negligible, the wave would have propagated several thousands of kilometers in the horizontal plane prior to our observation. However, if the horizontal background winds at lower altitudes were opposite to the wave propagation direction, the horizontal distance and time taken to reach the mesopause would be shorter [*Nicolls et al.*, 2010].

[36] The 7.7 h wave propagates approximately northward, which suggests the wave source is located across the Antarctic continent. As *Nicolls et al.* [2010] argued in analyzing the IGWs observed in the Arctic, a possible mechanism of IGW generation is geostrophic adjustment of the jet stream. In general, any "bulk" change to the background wind (at any altitude) will excite gravity waves [*Zhu and Holton*, 1987; *Vadas and Fritts*, 2001]; if this change takes more than a few hours and the horizontal scales are large, then IGWs will be excited. We can speculate (similar to *Nicolls et al.* [2010]) that the 7.7 h IGW observed at McMurdo was excited by geostrophic adjustment of the jet stream or unbalanced flow on the opposite side of the Antarctic continent. Work by *Sato et al.* [2012] utilized a high-resolution, middle-atmosphere, general circulation model to examine the gravity wave field in the Southern Hemisphere polar region. They found significant downward energy flux in the stratosphere during the winter. Their work suggests that at least some proportion of this field is linked to the in situ production of waves within the stratosphere. The existence of in situ wave sources in the stratosphere is also supported by *Sato and Yoshiki* [2008], *Yamashita et al.* [2009], and *Yamashita* [2011]. From intensive radiosonde observations performed at Syowa Station (69.0°S, 39.6°E), *Sato and Yoshiki* [2008] demonstrated that the IGWs observed in June were generated by spontaneous geostrophic adjustment of the unbalanced polar night jet located in the stratosphere. *Yamashita et al.* [2009] characterized gravity waves in the altitude range of 30–45 km at the South Pole (90°S) and Rothera (67.5°S, 68.0°W) with lidar data. They found that ~44% of the observed waves had upward phase progression, indicating downward wave propagation from the stratosphere or above. Using ECMWF data, *Yamashita* [2011] demonstrated that the wave excitation occurs in the stratosphere from in situ energy sources.

[37] Using a similar heuristic approach as in *Nicolls et al.* [2010] (that is, assuming constant horizontal and vertical group velocities and zero background wind), we can estimate approximate locations of the wave along its propagation path. We can then compare these locations with the structure of the background winds (at the appropriate locations and altitudes) from the MERRA reanalysis data. This will enable us to identify regions for which the background winds have significantly changed direction or speed in time over the period of 6–12 h and over scales of several hundreds of kilometers. In such regions, the air likely goes out of geostrophic imbalance, leading to the generation of inertia-gravity waves [*Zhu and Holton*, 1987; *Fritts and Luo*, 1992; *Luo and Fritts*, 1993; *Vadas and Fritts*, 2001]. These waves are generated because the air in those regions strives to regain geostrophic balance. Therefore, identifying regions of significant wind changes in the MERRA data allows us to identify regions where the IGWs could have been generated. (The MERRA data are available from the GES DISC website.)

[38] We examine the MERRA winds from 60 km (the approximate altitude of the highest MERRA pressure level output) to the surface at the times that the wave intersects that level. Inspection of the winds at the different altitude levels linked to the 7.7 h wave shows no features suggestive of unbalanced flow until the 0.7 and 1 hPa levels (43–46 km), as illustrated in Figure 11. In Figures 11a–11c, the stratospheric wind speeds are shown at 0.7 hPa (~46 km) on 28 June 2011 for 9, 12, and 15 UT, respectively. The open magenta circles show the estimated wave location of the 7.7 h wave at 12 UT. This location is approximately (67°S, 3°E), a distance of ~3900 km from McMurdo. (Note that these magenta circles are in identical locations.) Figures 11d–11f show the stratospheric wind speeds at 1 hPa on 28 June 2011 for 6, 9, and 12 UT, respectively. Here, the open magenta circles show the estimated wave location for the earlier time of 9 UT and at the slightly lower altitude of ~43 km. This location is approximately (65°S, 2°E), ~4100 km away from McMurdo. (Again, the magenta circles are in identical locations in Figures 11d–11f.) In the vicinity of each estimated wave position at the 0.7 and 1 hPa levels, we see what appears to be a jet stream exit region. In these regions and for both levels, the background winds change dramatically over a relatively short period of time. For 0.7 hPa, the background winds (u, v) are (74, 8) m/s at 9 UT on 28 June 2011, (79, 8) m/s at 12 UT, and then change significantly to (67, −13) m/s at 15 UT. The variations of the background winds are $(\Delta u, \Delta v) = (-7, -21)$ m/s over a period of 6 h. At 1 hPa, the variations of the background winds are

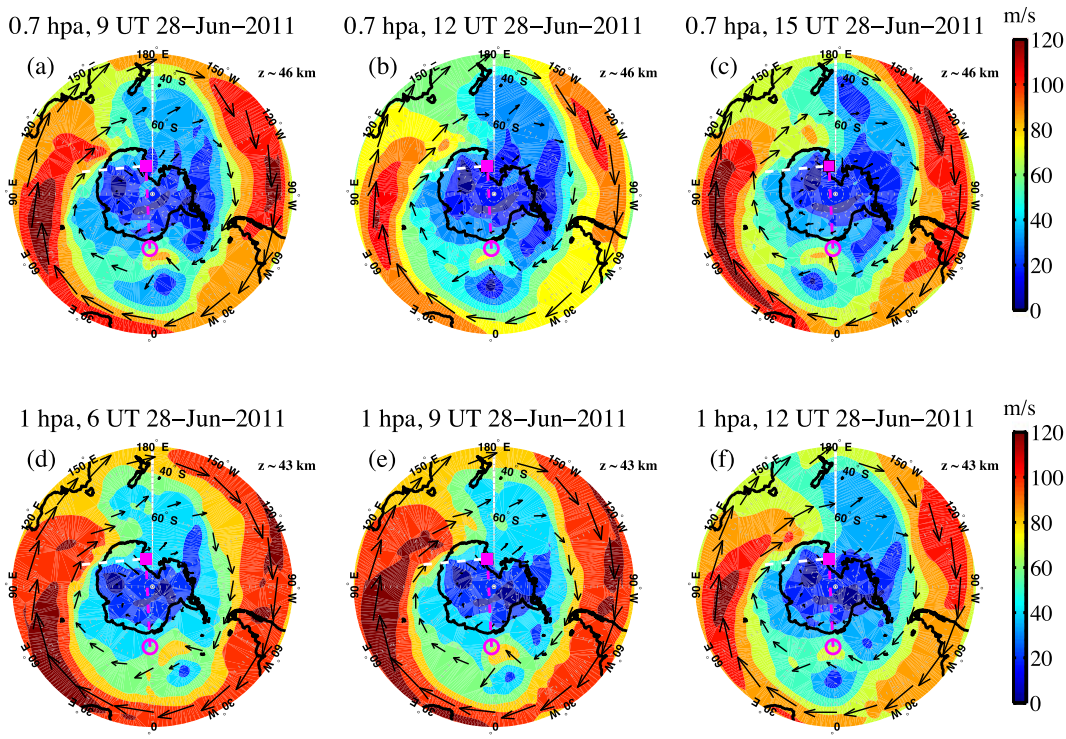

Figure 11. Horizontal winds over the Southern Hemisphere from the MERRA reanalysis data. Arrows are wind vectors, and colors denote wind speeds. The magenta solid square indicates McMurdo. The 0.7 hPa winds (~46 km) at (a) 9, (b) 12, and (c) 15 UT on 28 June 2011, respectively. The open magenta circles show the estimated wave location of the 7.7 h wave for 12 UT. The 1 hPa winds (~43 km) at (d) 6, (e) 9, and (f) 12 UT on 28 June 2011, respectively. The open magenta circles show the estimated wave location of the 7.7 h wave for the earlier time of 9 UT (which corresponds to the slightly lower altitude). White and magenta dashed lines show the estimated "zero-wind" horizontal trajectories of the 5 h and 7.7 h waves, respectively.

$(\Delta u, \Delta v) = (28, -13)$ m/s over the same length of time (but from 6 to 12 UT on 28 June 2011). These relatively rapid changes in the background winds can be modeled as an external body force, which excites IGWs that propagate in most directions (except those perpendicular to the body force) [e.g., *Vadas and Fritts*, 2001]. Studies by *O'Sullivan and Dunkerton* [1995] and *Thomas et al.* [1999] have also identified such regions as potential areas of active wave formation. Therefore, we hypothesize that the jet stream exit region at the level between 0.7 and 1 hPa, as indicated by the magenta open circles, may be the source of the 7.7 h wave. The large horizontal distance (~3900–4100 km) traveled by this wave is similar to that obtained by *Nicolls et al.* [2010] of ~4500–5500 km for the Arctic IGW. Note that the IGW observed by *Nicolls et al.* [2010] propagated southward over Alaska and was traced back to northern Russia. Therefore, the IGW in their case likely propagated over the Arctic, which is comparable to our case that the IGW propagated across the Antarctic continent to reach McMurdo. It is worth pointing out that the IGW in the Arctic case may have originated from a jet stream adjustment at $z \sim 10$ km near the tropopause [*Nicolls et al.*, 2010], while the stratosphere jet stream near 1 hPa (~43 km) is indicated in our Antarctic case as the wave source. Given the approximate north-south propagation direction of this 7.7 h wave and that the southward component of the background wind along the wave propagation path was smaller than the wave's phase velocity (not shown), we believe that this wave could have originated from this altitude range and could have followed this trajectory without being removed by critical-level filtering.

[39] The 5 h wave propagates nearly zonally from west to east. A similar analysis for the 5 h wave does not display a similarly convincing coincidence between the potential wave source and a region of unbalanced flow within the region observable by the MERRA reanalysis. However, given the zonal direction of wave propagation (denoted by white lines in Figure 11) and the high likelihood of critical-level filtering, we suggest that its source was more likely above the upper boundary of MERRA ($z \sim 60$ km).

6. Conclusions

[40] Combined Fe lidar/MF radar measurements have shown the presence of two independent IGWs observed simultaneously above Arrival Heights during 29–30 June 2011 for over 20 h in the Antarctic MLT. The two IGWs have ground-based observed periods of 7.7 ± 0.2 and 5.0 ± 0.1 h, respectively. Temporal filtering and hodograph analysis are applied to the temperature and wind data to determine the propagation directions of these IGWs. To resolve the ambiguity in the hodograph analysis, the phase difference between the temperature and horizontal wind perturbations (parallel to the horizontal wave propagation direction) is

derived; this serves as a constraint for the extracted azimuth angle of the propagation direction. The analysis results show that the 7.7 h wave propagates approximately northward, while the 5 h wave propagates approximately eastward; these directions are approximately perpendicular to each other. The intrinsic frequency and horizontal wave number of each wave are calculated via solving a quadratic equation derived from the linear dispersion and polarization relations. The intrinsic periods are estimated to be 7.9 ± 0.3 and 4.5 ± 0.3 h, and the corresponding horizontal wavelengths are $2.2 \pm 0.2 \times 10^3$ and $1.1 \pm 0.1 \times 10^3$ km, respectively. We have performed robust error analyses that have allowed us to derive the uncertainty in each IGW parameter.

[41] To our knowledge, this is the first known observation of two simultaneous IGWs in the MLT at the same location. It is also the first report of the coincident observations of IGWs by an MF radar and lidar in the Antarctic MLT region. The intrinsic horizontal phase speeds are determined to be 80 ± 4 and 68 ± 5 m/s for the 7.7 h and 5 h waves, respectively. For the 7.7 h IGW, its horizontal and vertical group velocities are 48 ± 3 and 0.5 ± 0.1 m/s, respectively. For the 5 h IGW, the horizontal and vertical group velocities are 58 ± 5 and 1.1 ± 0.1 m/s, respectively. Therefore, both waves propagate with very shallow elevation angles from the horizon: ~0.6° and 1.1° for the longer- and shorter-period waves, respectively. This implies that it would take 1–2 days for the waves to propagate to the MLT after traveling several thousands of kilometers in the horizontal plane prior to our observations. This would have placed the source of the 7.7 h wave (propagating meridionally) on the opposite side of the Antarctic continent. As *Nicolls et al*. [2010] proposed, we speculate that both IGWs observed at McMurdo were generated from similar mechanisms, i.e., the geostrophic adjustments of the jet stream or unbalanced flow, but from different sources around Antarctica. A simple analysis of MERRA reanalysis data shows strong circumstantial evidence for the 7.7 h IGW to be associated with a source in the stratosphere linked to a region of unbalanced flow. A complete investigation of the wave sources and generation mechanisms is beyond the scope of this paper, but is a subject for future work.

[42] Observation of two simultaneous IGWs is unusual, but single IGW events have been frequently observed in the lidar temperatures at McMurdo. For example, an IGW event was identified with an intrinsic period of 7.5 h on 11 July 2011 at McMurdo [*Chen et al*., 2012]. The lidar campaign in the last 2 years has revealed an unexpectedly high occurrence of IGWs in the Antarctic MLT region. Due to the expected low likelihood of IGWs propagating to the MLT region, the observed high occurrence rate indicates that Antarctica may have favorable conditions for the upward propagation of IGWs. Statistical studies and numerical modeling are crucial for improving our understanding of the sources and impacts of IGWs on the polar middle and upper atmosphere.

[43] **Acknowledgments.** We sincerely acknowledge Wentao Huang, Zhangjun Wang, John A. Smith, Brendan Roberts, and Chester S. Gardner for their significant contributions to the McMurdo lidar campaign. We are grateful to Anne Smith, Han-Li Liu, and Mike Nicolls for valuable discussions. We appreciate the staff of McMurdo Station and Scott Base for their superb support. We offer special thanks to Ed Butler of the Antarctica New Zealand and Vladimir Papitashvili of the National Science Foundation for their encouragement and help in this collaborative research. The lidar project is supported by the USA National Science Foundation OPP grant ANT-0839091. AJM thanks Antarctica New Zealand for the logistic support for the MF radar. SLV is supported by NSF grant AGS-1139149. We also acknowledge Global Modeling and Assimilation Office (GMAO) and the GES DISC for the dissemination of MERRA.

References

Alexander, M. J., and K. H. Rosenlof (2003), Gravity-wave forcing in the stratosphere: Observational constraints from the Upper Atmosphere Research Satellite and implications for parameterization in global models, *J. Geophys. Res.*, *108*(D19), 4597, doi:10.1029/2003JD003373.

Baumgaertner, A. J. G., A. J. McDonald, G. J. Fraser, and G. E. Plank (2005), Long-term observations of mean winds and tides in the upper mesosphere and lower thermosphere above Scott Base, Antarctica, *J. Atmos. Sol.-Terr. Phys.*, *67*, 1480–1496, doi:10.1016/j.jastp.2005.07.018.

Chen, C., X. Chu, Z. Yu, W. Fong, A. J. McDonald, X. Lu, and W. Huang (2012), Lidar and radar investigation of inertia gravity wave intrinsic properties at McMurdo, Antarctica, Proceedings of the 26th International Laser Radar Conference, 25–29 June 2012, Greece.

Chu, X., W. Pan, G. Papen, C. S. Gardner, and J. Gelbwachs (2002), Fe Boltzmann temperature LIDAR: Design, error analysis, and initial results at the North and South Poles, *Appl. Opt.*, *41*, 4400–4410.

Chu, X., and G. Papen (2005), Resonance fluorescence lidar for measurements of the middle and upper atmosphere, in Laser Remote Sensing, edited by T. Fujii and T. Fukuchi, pp. 179–432, CRC Press, Boca Raton, Fla.

Chu, X., C. S. Gardner, and S. J. Franke (2005), Nocturnal thermal structure of the mesosphere and lower thermosphere region at Maui, Hawaii (20.7°N), and Starfire Optical Range, New Mexico (35°N), *J. Geophys. Res.*, *110*, D09S03, doi:10.1029/2004JD004891.

Chu, X., W. Huang, F. Fong, Z. Yu, Z. Wang, J. A. Smith, and C. S. Gardner (2011a), First lidar observations of polar mesospheric clouds and Fe temperatures at McMurdo (77.8°S, 166.7°E), Antarctica, *Geophys. Res. Lett.*, *38*, L16810, doi:10.1029/2011GL048373.

Chu, X., Z. Yu, C. S. Gardner, C. Chen, and W. Fong (2011b), Lidar observations of neutral Fe layers and fast gravity waves in the thermosphere (110–155 km) at McMurdo (77.8°S, 166.7°E), Antarctica, *Geophys. Res. Lett.*, *38*, L23807, doi:10.1029/2011GL050016.

Chu, X., Z. Yu, C. Chen, F. Fong, W. Huang, C. S. Gardner, Z. Wang, B. Roberts, and J. A. Smith (2012), McMurdo lidar campaign: A new look into polar upper atmosphere, *26th International Laser Radar Conference*, 25–29 June 2012, Greece.

Collins, R. L. and C. S. Gardner (1995), Gravity wave activity in the stratosphere and mesosphere at the South Pole, *Adv. Space Res.*, *16*(5) 81–90.

Collins, R. L., D. C. Senft, and C. S. Gardner (1992), Observations of a 12 H wave in the mesopause region at the South Pole, *Geophys. Res. Lett.*, *19*(1), 57–60, doi:10.1029/91GL02780.

Collins, R. L., A. Nomura, and C. S. Gardner (1994), Gravity waves in the upper mesosphere over Antarctica: Lidar observations at the South Pole and Syowa, *J. Geophys. Res.*, *99*(D3), 5475–5485, doi:10.1029/93JD03276.

Cot, C., and J. Barat (1986), Wave-turbulence interaction in the stratosphere: A case study, *J. Geophys. Res.*, *91*(D2), 2749–2756, doi:10.1029/JD091iD02p02749.

Dörnbrack, A., T. Birner, A. Fix, H. Flentje, A. Meister, H. Schmid, E. V. Browell, and M. J. Mahoney (2002), Evidence for inertia gravity waves forming polar stratospheric clouds over Scandinavia, *J. Geophys. Res.*, *107*, 8287, doi:10.1029/2001JD000452.

Du, J., and W. E. Ward (2010), Terdiurnal tide in the extended Canadian Middle Atmospheric Model (CMAM), *J. Geophys. Res.*, *115*, D24106, doi:10.1029/2010JD014479.

Fraser, G. J. (1984), Summer circulation in the Antarctic middle atmosphere, *J. Atmos. Terr. Phys.*, *46*, 143–146, doi:10.1016/0021-9169(84)90139-9.

Friedman, J. S., and X. Chu (2007), Nocturnal temperature structure in the mesopause region over the Arecibo Observatory (18.35°N, 66.75°W): Seasonal variations, *J. Geophys. Res.*, *112*, D14107, doi:10.1029/2006JD008220.

Fritts, D. C., and M. J. Alexander (2003), Gravity wave dynamics and effects in the middle atmosphere, *Rev. Geophys.*, *41*(1), 1003.

Fritts, D. C., and Z. Luo (1992), Gravity wave excitation by geostrophic adjustment of the jet stream. Part 1: Two-dimensional forcing, *J. Atmos. Sci.*, *49*, 681–697.

Fritts, D. C., and P. K. Rastogi (1985), Convective and dynamical instabilities due to gravity wave motions in the lower and middle atmosphere: Theory and observations, *Radio Sci.*, *20*(6), 1247–1277, doi:10.1029/RS020i006p01247.

Fritts, D. C., and R. A. Vincent (1987), Mesospheric momentum flux studies at Adelaide, Australia—Observations and a gravity wave-tidal interaction model, *J. Atmos. Sci.*, *44*, 605–619.

Fritts, D. C., D. M. Riggin, B. B. Balsley, and R. G. Stockwell (1998), Recent results with an MF radar at McMurdo, Antarctica: Characteristics and variability of motions near 12-hour period in the mesosphere, *Geophys. Res. Lett.*, *25*(3), 297–300, doi:10.1029/97GL03702.

Gelbwachs, J. (1994), Iron Boltzmann factor LIDAR: Proposed new remote-sensing technique for mesospheric temperature, *Appl. Opt. 33*, 7151–7156 (1994).

Guest, F. M., M. J. Reeder, C. J. Marks, and D. J. Karoly (2000), Inertia-gravity waves observed in the lower stratosphere over Macquarie Island, *J. Atmos. Sci.*, *57*, 737–752.

Hall, G. E., C. E. Meek, and A. H. Manson (1995), Hodograph analysis of mesopause region winds observed by three MF radars in the Canadian Prairies, *J. Geophys. Res.*, *100* (D4), 7411–7421, doi:10.1029/95JD00195.

Hauchecorne, A. and M. Chain (1980), Density and temperature profiles obtained by lidar between 35 and 70 km, *Geophys. Res. Lett.*, *7*(8), 565–568, doi:10.1029/GL007i008p00565.

Hernandez, G., R. W. Smith, and J. F. Conner (1992), Neutral wind and temperature in the upper mesosphere above South Pole, Antarctica, *Geophys. Res. Lett.*, *19*(1), 53–56.

Hernandez, G., G. J. Fraser, and R. W. Smith (1993), Mesospheric 12-hour oscillation near South Pole, Antarctica, *Geophys. Res. Lett.*, *20*(17), 1787–1790, doi:10.1029/93GL01983.

Hoffmann, P., A. Serafimovich, D. Peters, P. Dalin, R. Goldberg, and R. Latteck (2006), Inertia gravity waves in the upper troposphere during the MaCWAVE winter campaign—Part I: Observations with collocated radars, *Ann. Geophys.*, *24*, 2851–2862.

Hu, X., A. Z. Liu, C. S. Gardner, and G. R. Swenson (2002), Characteristics of quasi-monochromatic gravity waves observed with Na lidar in the mesopause region at Starfire Optical Range, NM, *Geophys. Res. Lett.*, *29*(24), 2169, doi:10.1029/2002GL014975.

Kundu, P. (1990), Fluid Mechanics, 638 pp., Academic Press, San Diego.

Li, T., C.-Y. She, H.-L. Liu, T. Leblanc, and I. S. McDermid (2007), Sodium lidar–observed strong inertia-gravity wave activities in the mesopause region over Fort Collins, Colorado (41°N, 105°W), *J. Geophys. Res.*, *112*, D22104, doi:10.1029/2007JD008681.

Liu, H.-L. and J. W. Meriwether (2004), Analysis of a temperature inversion event in the lower mesosphere, *J. Geophys. Res.*, *109*, D02S07, doi:10.1029/2002JD003026.

Lu, X., A. Z. Liu, G. R. Swenson, T. Li, T. Leblanc, and I. S. McDermid (2009), Gravity wave propagation and dissipation from the stratosphere to the lower thermosphere, *J. Geophys. Res.*, *114*, D11101, doi:10.1029/2008JD010112.

Luo, Z., and D. C. Fritts (1993), Gravity wave excitation by geostrophic adjustment of the jet stream. Part II: Three-dimensional forcing, *J. Atmos. Sci.*, *50*, 104–115.

McDonald, A. J., S. E. George, and R. M. Woollands (2009), Can gravity waves significantly impact PSC occurrence in the Antarctic?, *Atmos. Chem. Phys.*, *9*, 8825–8840, doi:10.5194/acp-9-8825-2009.

McLandress, C., T. G. Shepherd, S. Polavarapu, and S. R. Beagley (2012), Is missing orographic gravity wave drag near 60°S the cause of the stratospheric zonal wind biases in chemistry–climate models?, *J. Atmos. Sci.*, *69*(3), 802–818, doi:10.1175/JAS-D-11-0159.1.

Nakamura, T., T. Tsuda, M. Yamamoto, S. Fukao, and S. Kato (1993), Characteristics of gravity waves in the mesosphere observed with the middle and upper atmosphere radar 2. Propagation direction, *J. Geophys. Res.*, *98*(D5), 8911–8923, doi:10.1029/92JD03030.

Nastrom, G. D., and F. D. Eaton (2006), Quasi-monochromatic inertia-gravity waves in the lower stratosphere from MST radar observations, *J. Geophys. Res.*, *111*, D19103, doi:10.1029/2006JD007335.

Nicolls, M. J., R. H. Varney, S. L. Vadas, P. A. Stamus, C. J. Heinselman, R. B. Cosgrove, and M. C. Kelley (2010), Influence of an inertia-gravity wave on mesospheric dynamics: A case study with the Poker Flat Incoherent Scatter Radar, *J. Geophys. Res.*, *115*, D00N02, doi:10.1029/2010JD014042.

Nielsen, K., M. J. Taylor, R. E. Hibbins, M. J. Jarvis, and J. M. Russell III (2012), On the nature of short-period mesospheric gravity wave propagation over Halley, Antarctica, *J. Geophys. Res.*, *117*, D05124, doi:10.1029/2011JD016261.

O'Sullivan, D., and T. J. Dunkerton (1995), Generation of inertia-gravity waves in a simulated life cycle of baroclinic instability, *J. Atmos. Sci.*, *52*, 3695–3716.

Sato, K. (1994), A statistical study of the structure, saturation and sources of inertio-gravity waves in the lower stratosphere observed with the MU radar, *J. of Atmos. Terr. Phys.*, *56* (6), 755–774. doi:10.1016/0021-9169(94)90131-7.

Sato, K., D. J. O'Sullivan, and T. J. Dunkerton (1997), Low-frequency inertia-gravity waves in the stratosphere revealed by three-week continuous observation with the MU radar, *Geophys. Res. Lett.*, *24*, 1739–1742.

Sato, K., S. Tateno, S. Watanabe, and Y. Kawatani, (2012), Gravity wave characteristics in the southern hemisphere revealed by a high-resolution middle-atmosphere general circulation model. *J. Atmos. Sci.*, *69*, 1378–1396, doi:10.1175/JAS-D-11-0101.1.

Sato, K., and M. Yoshiki (2008), Gravity wave generation around the polar vortex in the stratosphere revealed by 3 hourly radiosonde observations at Syowa Station, *J. Atmos. Sci.*, *65*, 3719–3735, doi:10.1175/2008JAS2539.1.

She, C. Y., *et al*. (2004), Tidal perturbations and variability in the mesopause region over Fort Collins, CO (41°N, 105°W): Continuous multi-day temperature and wind lidar observations, *Geophys. Res. Lett.*, *31*, L24111, doi:10.1029/2004GL021165.

Shibata, T., K. Sato, H. Kobayashi, M. Yabuki, and M. Shiobara (2003), Antarctic polar stratospheric clouds under temperature perturbation by nonorographic inertia gravity waves observed by micropulse lidar at Syowa Station, *J. Geophys. Res.*, *108*(D3), 4105, doi:10.1029/2002JD002713.

Smith, A. K., and D. A. Ortland (2001), Modeling and analysis of the structure and generation of the terdiurnal tide, *J. Atmos. Sci.*, *58*, 3116–3134.

States, R. J., C. S. Gardner (2000), Thermal structure of the mesopause region (80–105 km) at 40°N latitude. Part II: Diurnal variations, *J. Atmos. Sci.*, *57*, 78–92.

Tan, B., H.-L. Liu, and X. Chu (2011), Studying "cold pole" problem in WACCM and comparisons to lidar temperature morphology, paper presented at the American Geophysical Union (AGU) Fall Meeting, San Francisco, CA.

Thomas, L., R. M. Worthington, and A. J. McDonald (1999), Inertia-gravity waves in the troposphere and lower stratosphere associated with a jet stream exit region, *Ann. Geophysicae. 17*, 115–121.

Torrence, C. and G. P. Compo (1998), A practical guide to wavelet analysis, *Bull. Am. Meteorol. Soc.*, *79* (1), 61–78.

Tsuda, T., S. Kato, T. Yokoi, T. Inoue, M. Yamamoto, T. E. VanZandt, S. Fukao, and T. Sato (1990), Gravity waves in the mesosphere observed with the middle and upper atmosphere radar, *Radio Sci.*, *25*(5), 1005–1018, doi:10.1029/RS025i005p01005.

Vadas, S. L. and D. C. Fritts (2001), Gravity wave radiation and mean responses to local body forces in the atmosphere, *J. Atmos. Sci.*, *58*, 2249–2279.

Vadas, S. L. (2012), Compressible f-plane solutions to body forces, heatings, and coolings, and application to the primary and secondary-thermospheric gravity waves generated by a deep convective plume, J. Geophys. Res., minor revisions requested, revised version submitted 1/13, available at http://www.cora.nwra.com/~vasha/Vadas_2012.pdf

Vaughan, G., and R. M. Worthington (2007), Inertia-gravity waves observed by the UK MST radar, *Q. J. R. Meteorol. Soc.*, *133*: (S2) 179–188.

Vincent, R. A. (1994), Gravity-wave motions in the mesosphere and lower thermosphere observed at Mawson, Antarctica, *J. Atmos. Terr. Phys.*, *56*, 593–602.

Vincent, R. A., and M. J. Alexander (2000), Gravity waves in the tropical lower stratosphere: An observational study of seasonal and interannual variability, *J. Geophys. Res.*, *105*, 17,971–17,982, doi:10.1029/2000jd900196.

Wang, Z., Z. Liu, L. Liu, S. Wu, B. Liu, Z. Li, and X. Chu (2010), Iodine-filter-based mobile Doppler lidar to make continuous and full-azimuth-scanned wind measurements: data acquisition and analysis system, data retrieval methods, and error analysis, *Appl. Opt.*, *49*, 36, 6960–6978.

Wang, Z., X. Chu, W. Huang, W. Fong, J. A. Smith, and B. Roberts (2012), Refurbishment and upgrade of Fe Boltzmann/Rayleigh temperature lidar at Boulder for a McMurdo lidar campaign in Antarctica, *Proceedings of the 26th International Laser Radar Conference*, 25–29 June 2012, Greece.

Xu, J., A. K. Smith, and G. P. Brasseur (2000), The effects of gravity waves on distributions of chemically active constituents in the mesopause region, *J. Geophys. Res.*, *105*(D21), 26,593–26,602, doi:10.1029/2000JD900446.

Yamashita, C., X. Chu, H.-L. Liu, P. J. Espy, G. J. Nott, and W. Huang (2009), Stratospheric gravity wave characteristics and seasonal variations observed by lidar at the South Pole and Rothera, Antarctica, *J. Geophys. Res.*, *114*, D12101, doi:10.1029/2008JD011472.

Yamashita, C. (2011), Atmospheric coupling through gravity waves during stratospheric sudden warmings: Gravity wave variations, generation mechanisms and impacts, PhD thesis, 151 pp., Dep. of Aerospace Eng. Sci., Univ. of Colorado Boulder, Boulder, Colorado, USA.

Zhu, X. and J. R. Holton (1987), Mean fields induced by local gravity-wave forcing in the middle atmosphere, *J. Atmos. Sci.*,*44*, 620–630.